Closed-loop Feedback Control of Microfluidic Cell Manipulation via Deep-learning Integrated Sensor Networks

Ningquan Wang,[a] Ruxiu Liu,[a] Norh Asmare,[a] Chia-Heng Chu,[a] Ozgun Civelekoglu,[a] and A. Fatih Sarioglu[*abc]

[a] School of Electrical and Computer Engineering, Georgia Institute of Technology, Atlanta, GA 30332, United States
[b] Parker H. Petit Institute for Bioengineering and Bioscience, Georgia Institute of Technology, Atlanta, GA 30332, United States
[c] Institute for Electronics and Nanotechnology, Georgia Institute of Technology, Atlanta, GA 30332, United States

Abstraction

Microfluidic technologies have long enabled the manipulation of flow-driven cells *en masse* under a variety of force fields with the goal of characterizing them or discriminating the pathogenic ones. On the other hand, a microfluidic platform is typically designed to function under optimized conditions, which rarely account for specimen heterogeneity and internal/external perturbations. In this work, we demonstrate a proof-of-principle adaptive microfluidic system that consists of an integrated network of distributed electrical sensors for on-chip tracking of cells and closed-loop feedback control that modulates chip parameters based on the sensor data. In our system, cell flow speed is measured at multiple locations throughout the device, the data is interpreted in real-time via deep learning-based algorithms, and a proportional-integral feedback controller updates a programmable pressure pump to maintain a desired cell flow speed. We validate the adaptive microfluidic system with both static and dynamic targets and also observe a fast convergence of the system under continuous external perturbations. With an ability to sustain optimal processing conditions in unsupervised settings, adaptive microfluidic systems would be less prone to artifacts and could eventually serve as reliable standardized biomedical tests at the point of care.

Keyword

Feedback control; Microfluidics; Coulter sensing; Deep learning; Sensor network; Cell tracking;

1. Introduction

Manipulation of suspended cells in microfluidic channels forms the basis of microchip-based sample enrichment and biomedical assays[1]. Those devices are specifically engineered to subject flow-driven cell populations to a variety of force fields (*e.g.*, mechanical,[2] electrical,[3] acoustic,[4] magnetic,[5] chemical,[6] *etc.*) and discriminate them based on the contrast in their biophysical[7] or biochemical[8] properties. As such, microfluidic devices are advantageous over conventional sample processing technologies due to their flexibility to implement highly selective and sensitive cell manipulation schemes that can detect even the scarcest of cells as circulating tumor cells (CTCs),[9,10] hematopoietic stem cells (HSCs),[11] and circulating fetal cells (CFCs)[12] among billions of normal blood cells.

While highly effective in manipulating cells, microfluidic devices are designed and experimentally optimized to operate under well-controlled conditions that cannot universally be maintained in practice.[13,14] Inevitable perturbations to device operation such as variation in the flow rate due to clogged channels[15] or fabrication-related deviations in device geometry[32] could go unnoticed and translate into process artifacts. Moreover, differences between sample viscosities[16] could lead to different flow dynamics[17,18] even if the rest of the operation parameters could be made equal. Therefore, microfluidic devices for cell analysis need to be engineered to preempt those potential artifacts due to process/sample variance if they were to be deployed in the field for biomedical applications.

One strategy to ensure the microfluidic device operates under optimized conditions irrespective of unforeseen perturbations is to employ a feedback control. A feedback-controlled system automatically regulates a process variable by constantly monitoring instantaneous changes (i.e., error) and countering those by triggering a negating stimulus to maintain that process variable at a set value.[19] Establishing a feedback control on a microfluidic therefore requires a quantitative assessment of the state of the device, a control algorithm (i.e., controller), and a control input to the system to change its state. In fact, feedback control has been successfully demonstrated in regulating microfluidic systems for a variety of applications, including digital microfluidics,[20-22] productions of micro-droplets,[23] modulations of fluidic properties,[24,25] and automated regulations of fluid height,[26] pressure,[27] and temperature[28] in microfluidic chambers.

Here, we demonstrate a system where the process variable is controlled within a feedback loop based on direct measurements on cells being manipulated within a microfluidic chip. Our system utilizes (1) a network of electrical sensors distributed across the microfluidic device to make measurements on flowing cells, (2) a trained deep learning algorithm to process the raw sensor data and produce actionable control signals, and (3) a controller that updates external stimuli to regulate the process variable. In a proof-of-principle demonstration, we measure cell flow speeds across the device and control a programmable pressure pump to maintain the same flow speed irrespective of perturbations. We characterize the system performance under static and dynamic perturbations and demonstrate its stability.

2. Results

2.1 System overview

The introduced adaptive microfluidic system was composed of three main units: the sensing unit, the signal processing unit, and the feedback control unit (Figure 1).

The sensing unit was a microfluidic sensor platform consisted of surface micro-electrodes, which were designed to produce electrical signals when a cell was detected. To detect cells within the device, we utilized the fact that suspended cells modulated the electrical current as they flowed over these microelectrodes. To monitor the cell flow throughout the whole device, we created a network of sensors distributed to multiple measurement nodes. Because all sensors were electrically connected, the data from the network could be acquired as a single

time waveform. Nevertheless, by designing each sensor to produce a distinct waveform, we ensured a lossless recovery of information from individual sensors in the recorded electrical signal.

The signal processing unit acquired raw sensor data, analyzed its content, and calculated parameters such as size, instantaneous location, and speed for every cell. The signal processing unit could be considered as a combination of a data acquisition block and a data interpretation block. The data acquisition block consisted of signal acquisition software and hardware, including amplifiers and a data acquisition board, which extracted, amplified, and transmitted sensor waveforms in real-time. Conditioned sensor waveforms were then processed by the data interpretation block. The sensor waveforms were analyzed using a deep-learning model specifically to perform cell measurements in real-time. Real-time analysis of sensor data then allowed timely intervention by the controller to modulate the device settings.

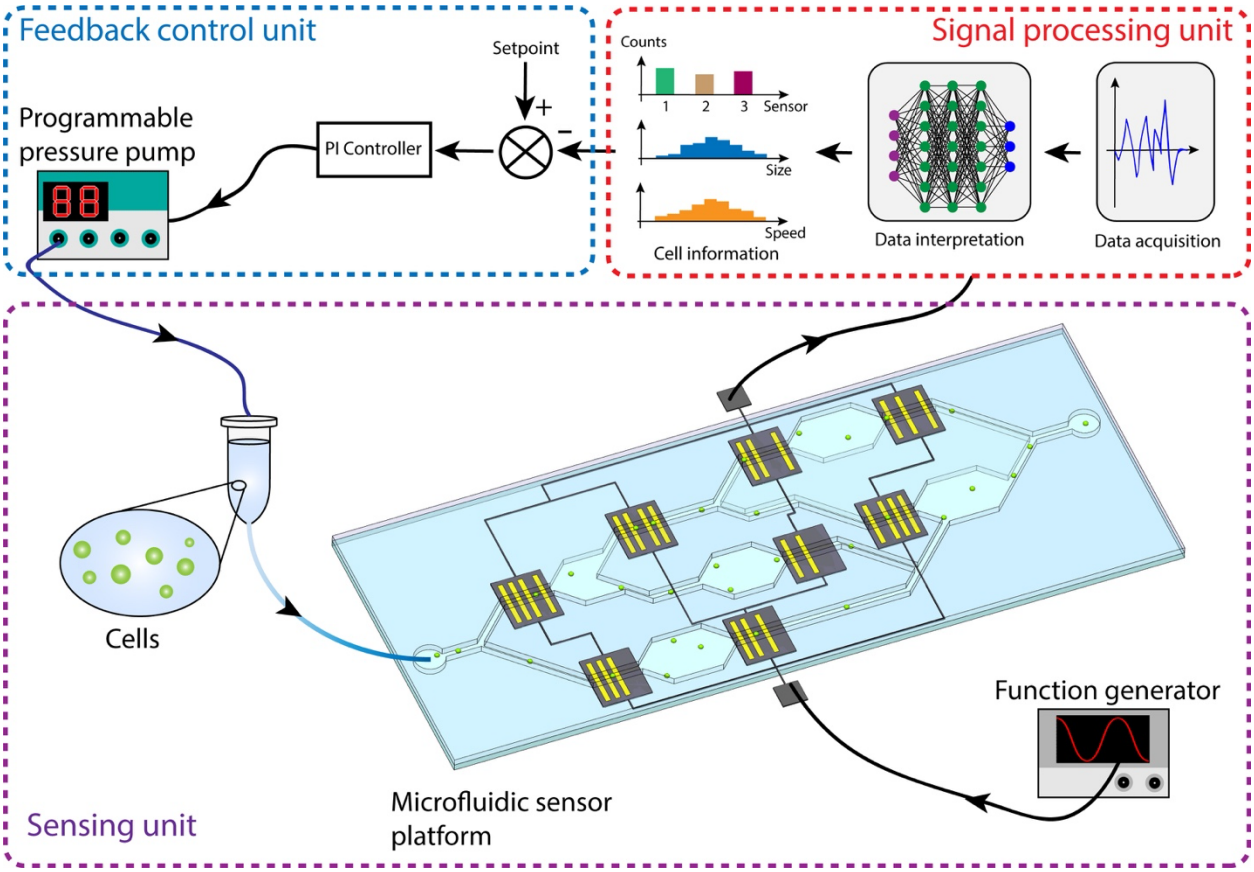

Figure 1: A concept illustration showing the workflow of the adaptive microfluidic system. A feedback loop is constructed among a sensing unit, a signal processing unit, and a feedback control unit. Target cells are manipulated and detected in the sensing unit, and cell information is extracted and interpreted in the signal processing unit. The feedback control unit regulates a process variable based on measured cell parameters and a predetermined setpoint.

The feedback control unit regulated a process variable based on the measurements on cells. Measured cell parameters were compared to a predetermined target value (setpoint), and the

process variable was continuously updated to minimize the difference between the two. In this work, we set our feedback loop on the cell flow speed without loss of any generality and updated the driving pressure of the sample by controlling a pressure pump. A regulated flow ensured cells to flow at a determined speed inside the device irrespective of external perturbations or potential miscalibration of the pressure pump or device geometry.

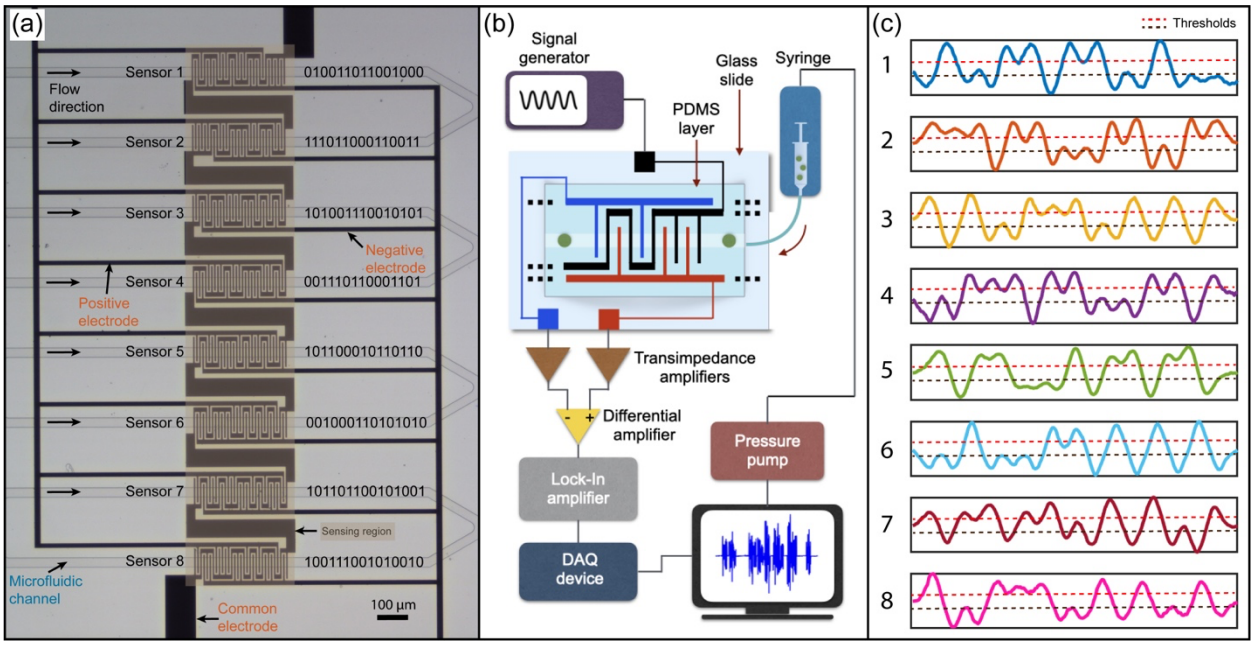

Figure 2: Microfluidic sensor platform design and experimental set-up. (a) A microscopy image of the microfluidic sensor platform with eight code-multiplexed Coulter sensors. Each sensor is designed with a unique electrode pattern determined by a distinct binary code sequence. (b) A block diagram for the experimental set-up. (c) The signature waveform for each coded sensor. The pattern of each signature waveform follows the corresponding binary code sequence. The threshold values used to determine positive and negative peaks are ± 0.05 mV.

2.2 Design of the sensing unit

We designed our microfluidic sensor platform based on the Microfluidic CODES technology, which allows spatiotemporal tracking of cells in microfluidic channels.[29-33] The Microfluidic CODES sensor network operated based on the Coulter principle, which had long been employed for counting and sizing cells in suspension.[34] However, unlike a conventional Coulter counter, Microfluidic CODES employed specially-micromachined electrodes to produce distinct electrical waveforms for code-multiplexed measurements from different locations on a microfluidic platform so as to track cells' movement.

Our sensor network was composed of eight coded Coulter sensors distributed to monitor eight 30 µm-wide microfluidic channels. Each sensor was designed to produce a unique binary sequence, specifically a randomly-generated 15-bit code sequence, i.e., each bit was treated as a Bernoulli random variable with p = 0.5 (Figure 2a). It should be noted that, these eight sensors were placed next to each other on the actual device, different from the format shown in the

concept illustration (Figure 1), so that the whole network could fit in the field-of-view of a microscope for an independent optical inspection while validating the system. To build the distributed sensors, we micromachined three coplanar electrodes, a common electrode, a positive electrode, and a negative electrode. The common electrode drove the sensors, while the positive and negative electrodes were used to measure impedance variations when cells flowed by. To encode a specific Coulter sensor, positive and negative electrodes were first patterned on either side of a microfluidic channel, and in the sensing region, the electrodes were arranged as an interdigitated array with 5 µm-wide electrode fingers separated by 5 µm-wide gaps. Specifically, electrode fingers were extended from each electrode and across the microfluidic channel, and the polarity (positive or negative) order of the electrode fingers was determined by the corresponding binary code sequence to be implemented. For example, a '1' in the code sequence indicated a positive electrode finger, a '0' in the code sequence indicated a negative electrode finger. Finally, the common electrode was routed in between the coding electrode fingers to drive the electrical current flow. In this case, when a cell flowed through a microfluidic channel equipped with one of these sensors, sequential interaction of the cell with electrode fingers induced a signature waveform that resembled a specific binary code dictated by the underlying electrode pattern.

To fabricate the sensor network, a 1.2 µm-thick negative photoresist (NR9-1500PY, Futurrex, Inc.) was spin-coated on a glass substrate and exposed using a maskless photolithography system (MLA150, Heidelberg Instruments). A 20/480 nm Cr/Au film stack was deposited on the developed photoresist using e-beam evaporation. Finally, the glass substrate was immersed in acetone to lift-off the sacrificial photoresist to create the electrode pattern and then diced into individual chips. Microfluidic channels over the sensor network were fabricated using soft lithography. A mold was first created by spin-coating a 15 µm-thick SU-8 photoresist (MicroChem) on a 4-inch silicon wafer and patterned using the same maskless photolithography system. Polydimethylsiloxane (PDMS) prepolymer (Sylgard 184, Dow Corning) was mixed with its crosslinker at a 10:1 ratio and then poured on the mold, degassed, and baked at 65 °C for >4 hours. Then, the cured PDMS was peeled off from the mold and punched using a biopsy punch to create the fluidic inlet and outlet. Finally, to form the device, the glass substrate and PDMS layer were activated in an oxygen plasma, aligned, and bonded.[35]

Sensors were tested using human breast cancer cells (MDA-MB-231). The cells were cultured in culture media (Mediatech; Cellgro, Herndon, VA) supplemented with 10% fetal bovine serum (FBS; Seradigm, Radnor, PA) and maintained in 5% CO2 atmosphere at 37 °C in an incubator. The cells were harvested once they reached >80% confluence by treating with trypsin, pelleting by centrifugation, and resuspending in phosphate buffered saline (PBS) with gentle pipetting. The cell suspension was driven through the microfluidic device with a programmable pressure pump (MFCS-EZ, Fluigent). The sensors were excited with a 460 kHz sine wave (2 V_{pp}) applied to the common electrode (Figure 2b). The excitation frequency was specifically chosen to (1) bypass the double-layer capacitance at the electrode-electrolyte interface, which was dominant at the low-frequency band and (2) prevent the Maxwell-Wagner dispersion at the high-frequency band.[36] Two electrical current signals were acquired from the positive and negative electrodes, converted into voltage signals through transimpedance amplifiers and combined

with a differential amplifier. A lock-in amplifier (HF2LI, Zurich Instruments) was used to demodulate the differential signal and measured the electrical current amplitude. The final output signal was sampled into a computer through a data acquisition (DAQ) device (PCIe-6361, National Instruments) at a sampling rate of 57 kHz. Signature waveforms corresponding to different locations on the chip were experimentally confirmed to match with the corresponding binary code sequences (Figure 2c).

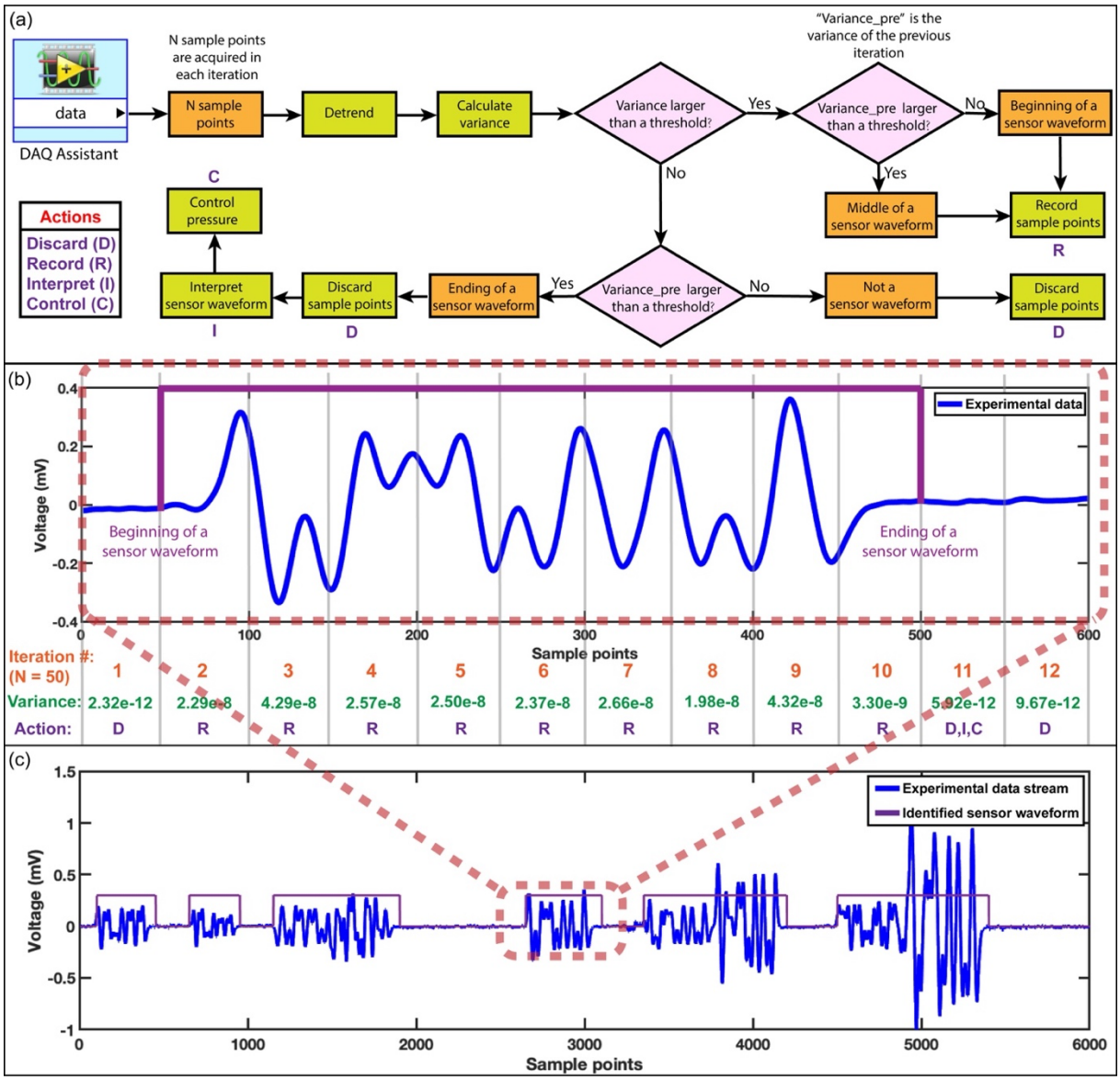

Figure 3: Real-time sensor waveform identification. (a) A flow diagram illustrating the environment implemented for real-time sensor waveform identification and extraction. (b) An illustration of the process of identifying a sensor waveform. For each data block, containing 50 sample points, the variance is calculated to determine whether the data block belongs to a sensor waveform or not. (c) Multiple sensor waveforms are successfully identified from an experimental data stream.

2.3 Design of the signal processing unit

2.3.1 Real-time signal processing environment

We developed a real-time signal processing environment that could continuously acquire, identify, and extract sensor waveforms corresponding to individual cell events (Figure 3a). Because cells randomly interacted with sensors at different locations, the sensor waveforms asynchronously appeared in the data stream (Figure 3c). To make the information available to the controller in a timely fashion, we continuously screened short blocks (50 samples) from the data stream to catch potential sensor activity. For each data block (iteration), we first calculated signal power (i.e., variance) and compared it with a predefined threshold value (variance of the baseline noise) to determine whether the signal in the current data block originated from a triggered sensor or was simply noise. If it were scored as sensor data, these samples would be temporarily stored in a buffer. Next, by comparing the current data block's signal variance with that of the previous data block, we determined if the data block corresponded to either beginning or ending of a sensor waveform. If the data block was identified as an ending block, all the data blocks stored in the buffer were combined and marked as a complete sensor waveform to be identified, followed by clearing the buffer for the next sensor waveform (Figure 3b).

We implemented the continuous data acquisition in LabVIEW, and the PyDAQmx package[37] was used as a software interface between the data acquisition board and Python, a programming language commonly employed for machine learning-based data analysis.[38] An off-line simulation of the signal extraction scheme demonstrated that sensor waveforms with varying amplitudes and durations were successfully identified from a recorded sensor data stream (Figure 3c). It should be noted that some of these extracted sensor waveforms were individual ones induced by a single cell, and some were interfering ones induced by coincident cells interacting with one or multiple sensors simultaneously. The pattern of individual sensor waveforms closely followed the binary code sequences used to encode each sensor so that they could readily be recognized, while interfering sensor waveforms required specific algorithms to demultiplex and interpret the cell information.

2.3.2 Deep learning-based data interpretation

The data interpretation block was designed based on the deep neural network (DNN),[39] which is a machine learning model commonly used for signal processing.[40-42] Specifically, our model was based on the convolutional neural network (ConvNet),[43,44] a type of deep neural network that is particularly well suited for processing data with a spatial or temporal dependency, such as images, videos, and speech signals. In the case of processing our sensor network data, the extracted sensor waveforms contained one or multiple signature waveforms, and each signature waveform had a specific pattern (spatial dependency). Therefore, we analogized our data interpretation process as an object detection process in 1-dimension, where each signature waveform was an object, and the entire extracted sensor waveform was the background image. The goal of the data interpretation block was to identify and recognize all the signature waveforms from an extracted sensor waveform, even when multiple signature waveforms interfered with each other due to coincidentally detected cells.

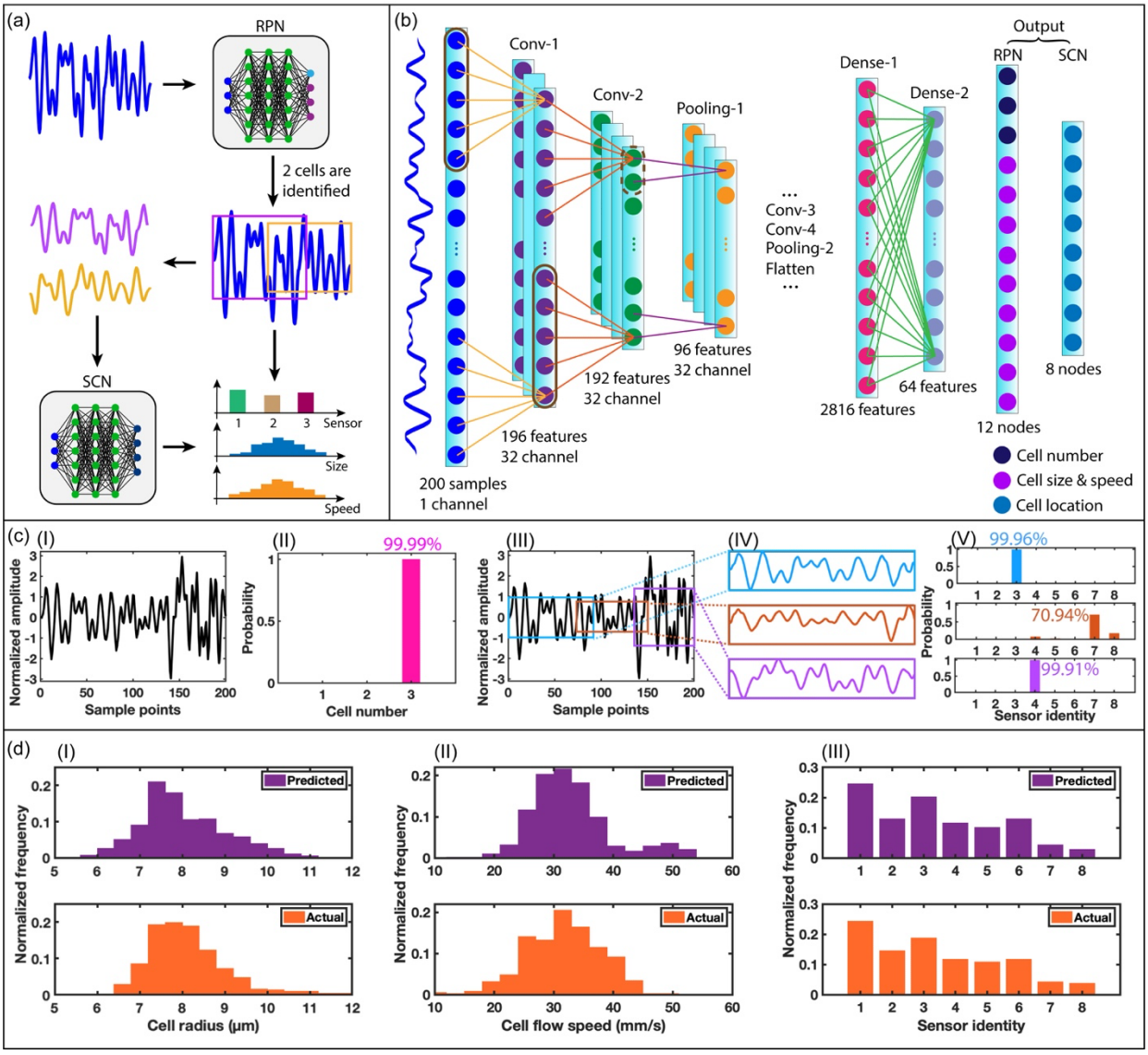

Figure 4: Implementation of the deep learning-based sensor waveform interpretation. (a) A workflow showing the decoding process of the 2-stage ConvNet model. Given an input sensor waveform, the first stage ConvNet (RPN) predicts the number of contained signature waveforms (cells) and fits a bounding box for each of them. The second stage ConvNet (SCN) predicts the sensor identity of each identified signature waveform. (b) The structure of the ConvNet model. The RPN and SCN share the same structure for feature extraction and have different output layers. (c) ConvNet decoding process for a representative 3-cell interfering sensor waveform from the validation dataset. (I). Three signature waveforms (cells) (II) and three bounding boxes (III) are identified and estimated by the PRN. Extracted and normalized signature waveforms (IV) are interpreted by the SCN for sensor identity prediction (V). (d) Validation of the ConvNet model through the test dataset with simultaneously acquired high-speed microscopy images. The predicted cell properties (from the ConvNet model) are compared with actual ones (from microscopy images) in terms of distributions of (I) cell radius, (II) cell flow speed, and (III) sensor identity.

We implemented a 2-stage ConvNet structure to interpret extracted sensor waveforms (Figure 4a). Given an input sensor waveform, the first stage, named region proposal network (RPN), predicted the number of signature waveforms contained in that waveform (e.g., 1 if isolated signature waveform or >1 if the sensor waveform resulted from the interference of multiple signature waveforms) and proposed a bounding box on each individual signature waveform. Each identified signature waveform was then extracted and fed into the second stage, named sensor classification network (SCN), for a further sensor identity (location) classification. Combining the predictions from two stages, the property and behavior of detected cells were estimated. First, the number of identified signature waveforms indicated the number of detected cells. Second, the height of the bounding box represented the amplitude of the signature waveform, which, based on the Coulter principle[45,46] was proportional to the size (volume) of the detected cell. Third, the width of the bounding box represented the duration of the signature waveform, which represented the time the cell spent passing through the entire sensing region of the corresponding sensor (cell residence time). This could be further used to calculate the speed of the cell. Fourth, the predicted sensor identity provided the location information of the cell as sensors were distributed at different locations on the microfluidic sensor platform. All of this information provided an on-demand snapshot of the state of cell manipulation within the microfluidic device.

In our ConvNet model, the RPN and the SCN shared the same structure for feature extraction, while each had a distinct output layer (Figure 4b). Specifically, each ConvNet contained four convolutional layers, each of which was followed by a ReLU layer for a non-linear activation. After the second and fourth convolutional layers, a max-pooling layer was placed to down-sample the feature map. Two dense (fully-connected) layers were placed after the second max-pooling layer (right before the output layer). The output layer of the RPN had two groups of nodes, where the first group predicted the number of contained signature waveforms in the input sensor waveform, and the second group fitted a bounding box for each identified signature waveform. The output layer of the SCN had eight nodes, each representing one of the eight distributed Coulter sensors on the microfluidic device. A more detailed illustration of the ConvNet model can be found elsewhere.[43]

To train our model, we built a dataset of 1,000,000 training sensor waveforms. In the training dataset, each sensor was uniformly represented by an approximately equal number of waveforms. Among those sensor waveforms, 1/3 were non-interfering sensor waveforms, 1/3 were 2-cell interfering sensor waveforms, and 1/3 were 3-cell interfering sensor waveforms. To increase the number of waveforms available for constructing the training dataset, we employed a data augmentation process. Briefly, each interfering training waveform was manually combined from randomly-scaled non-interfering sensor waveforms. A detailed illustration of this data augmentation process can be found elsewhere.[43]

After training both ConvNets for 50 epochs (Figure S1), we first generated a validation dataset. The validation dataset was digitally constructed with the interfering sensor waveforms manually composed by combining labeled but unseen non-interfering sensor waveforms recorded from previous experiments. Therefore, for each waveform in the validation dataset,

we knew the ground truth in terms of the number of coincident cells, dimensions of the bounding boxes, and sensor identities. Using the generated validation dataset, we then investigated the decoding process and evaluated the performance of ConvNets (Figure 4c). For each sensor waveform (Figure 4c, I), the RPN predicted the number of signature waveforms (cells) producing the observed signal with a confidence level (Figure 4c, II) and marked individual signature waveforms making up the signal with bounding boxes (Figure 4c, III). Once the signature waveforms within the bounding boxes were extracted and normalized (Figure 4c, IV), the SCN made a sensor identity prediction on each identified signature waveform and reported the confidence level for each prediction (Figure 4c, V). By processing all waveforms in the validation dataset, we calculated the accuracy of our ConvNets in recognizing sensor waveforms (Figure S2).

Next, we constructed a test dataset, which contained signals as recorded from processed cells on the device. For the signals in the test dataset, we simultaneously recorded high-speed microscopy images of interaction of cells with the sensors. We then processed recorded images to extract information as the ground truth and compared the ConvNets-predicted measurements with image-based data to assess accuracy in terms of predicting cell size, speed, and sensor identity (Figure 4d).

2.4 Design of the feedback control unit

2.4.1 Design of the feedback control system

To demonstrate closed-loop control of cell manipulation in the microfluidic device, we developed a feedback control system that regulated cell flow speed based on measurements on processed cells. Besides the fact that cell flow speed is of practical importance for a variety of cell manipulation/sorting applications in microfluidic devices,[47] it has a simple dependence on the driving pressure, making it an ideal parameter for proof-of-concept demonstration of closed-loop control. The designed feedback control system could be abstracted into a plant and a feedback controller (Figure 5a). The plant consisted of the programmable pressure pump, the sensing unit, and the signal processing unit producing a measured process variable, $y(t)$, which was the variable to be controlled in the system. The goal of the feedback control system was to regulate the control input (the pump pressure), so that the process variable could approach the setpoint, $r(t)$, as the target value of the process variable. This was achieved by the system continuously calculating an error value, $e(t)$, as a difference between the instantaneous process variable and the setpoint and the feedback controller attempting to minimize the error by generating an appropriate adjustment value, $u(t)$, to update the control input in the plant.

The core part of our feedback control system was the feedback controller, which determined the parameters adjusting the control input given a specific error value. For our study, we implemented a proportional-integral (PI) controller, which adjusted the control input based on a weighted sum of present and past error values.[48] As such, the adjustment value to the pressure pump was computed by

$$u(t) = Ke(t) + \frac{K}{T_i}\int_0^{T_i} e(\tau)d\tau$$

where K was the feedback gain, and T_i was the integration period.

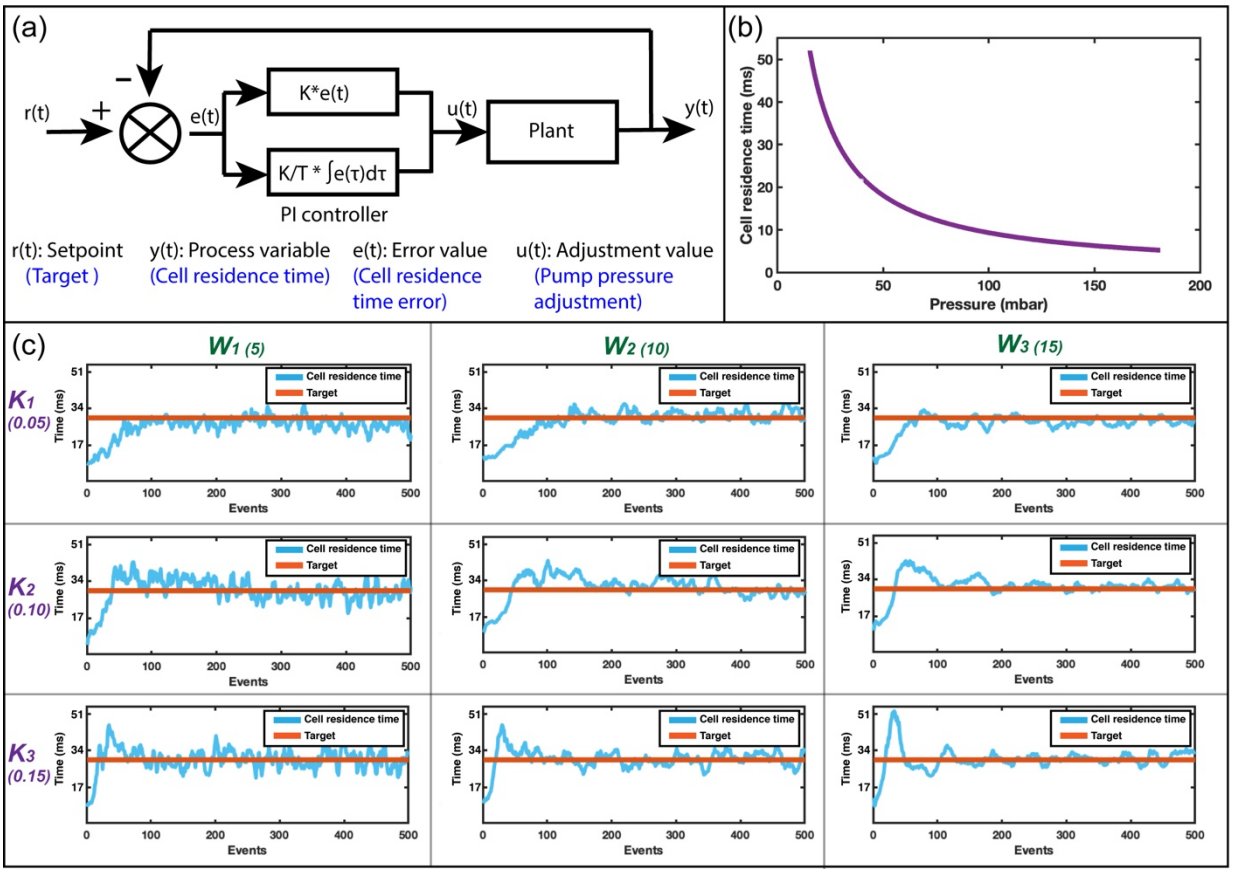

Figure 5: Design and characterization of the feedback control system. (a) A block diagram showing the proportional-integral (PI) controller in the microfluidic feedback control system. The cell residence time is selected as the process variable. (b)The monotonic relation between the pump pressure and the cell residence time. (c) Step response of the feedback control system given different combinations of feedback gain (K) and averaging window size (W), in which K_1 = 0.05, K_2 = 0.10, K_3 = 0.15, and W_1 = 5, W_2 = 10, W_3 = 15.

To regulate the cell flow speed in a feedback control loop, we chose the measured time that a cell interacted with a sensor (cell residence time) as the process variable. The cell residence time was inversely proportional to the cell flow speed, which had a linear relationship with the driving pressure (Figure S3). Therefore, the cell residence time had a non-linear but monotonic relation with the driving pressure and hence could be adjusted by updating the pressure pump settings (Figure 5b). Each time a cell (i.e., event) was detected, our system measured the cell residence time, compared it with the setpoint, and calculated an error value, based on which, the PI controller produced an updated setting for the programmable pressure pump.

2.4.2 Step response of the feedback control system

To characterize our feedback control system, we processed a model biological sample with a density of 0.5 x 10^6 cells/ml. We first measured the step response of the system. In these measurements, we set the setpoint for cell residence time at 10 ms, corresponding to a pressure of 95 mbar. Then we abruptly changed the setpoint from 10 ms to 30 ms and monitored changes in the process variable as it converged to the new setpoint (Figure 5c). We analyzed the effects of the feedback gain (K) and the averaging window size (W), which set the number of earlier cell measurements considered when calculating the instantaneous cell residence time. Specifically, we set K as 0.05, 0.10 or 0.15 and W as 5, 10 or 15 and tested their combinations. For each parameter combination, we evaluated the step response against multiple metrics: First, we measured the rise time, defined as the number of events required for the cell residence time to rise from 10% to 90% of the setpoint, indicating how fast the system responded to a change in the setpoint. Second, we measured the settling time from the number of events required for the cell residence time to enter and stay within a certain error band (15%) around the setpoint, indicating how fast the system converged. Note that because our measurements were only updated when a cell was detected by the sensor network, we chose our unit of progress as the cell detection events rather than the actual time commonly used in these analyses. Finally, we analyzed the response in its overshoot from how much the cell residence time exceeded the new setpoint before convergence, representing the maximum swing of the control system.

Analysis of step responses from different feedback controller clearly showed the effect of varying feedback parameters. Increasing the feedback gain resulted in a faster response due to a higher sensitivity to the error value but also led to larger swings and a less stable system. With a higher K, the rise time decreased, the overshoot increased, and the settling time increased (Table 1), an expected response from a PI controller.[48] Varying the W, on the other hand, acted as a noise filter for cell residence time measurements. Because cell flow speed within a microfluidic device had an intrinsic variance due to Poiseuille flow profile[49] within channels or non-uniform hydraulic resistance across the device, averaging measurements over multiple cells reduced noise in calculated error values. This resulted in a smoother response but increased the time to convergence (Figure 5c).

K	Rise time (events)	Overshoot (ms)	Settling time (events)
0.05	55	3.4	73
0.10	31	13.3	171
0.15	18	23.1	188

Table 1: The effect of the feedback gain (K) on the rise time, overshoot, and settling time of the system for W = 15.

2.4.3 Tracking of dynamic setpoints

Next, we tested our system's ability to follow a varying setpoint for the process variable. A dynamic setpoint for a process variable could be helpful in practice for applications where sweeping operational settings of a microfluidic device could enable a parametric analysis on a sample.[50-52] In characterizing our system for dynamic setpoints, we chose a K of 0.1 and a W of 5 to build the feedback controller. We programmed the setpoint to vary with a controlled pattern and monitored how well the instantaneous cell residence time in the microfluidic device followed the programmed function (Figure 6). We first ramped the cell residence time from 10 ms to 30 ms and found that the system was able to track the setpoint successfully (Figure 6a). Next, we modulated the setpoint sinusoidally, and the system was able to respond with a small but noticeable delay (Figure 6b). Finally, we modulated the setpoint in the form of a square wave. While we clearly observed the feedback delay and ringing on both rising and falling edges, the system recovered in between and was able to track the setpoint successfully (Figure 6c).

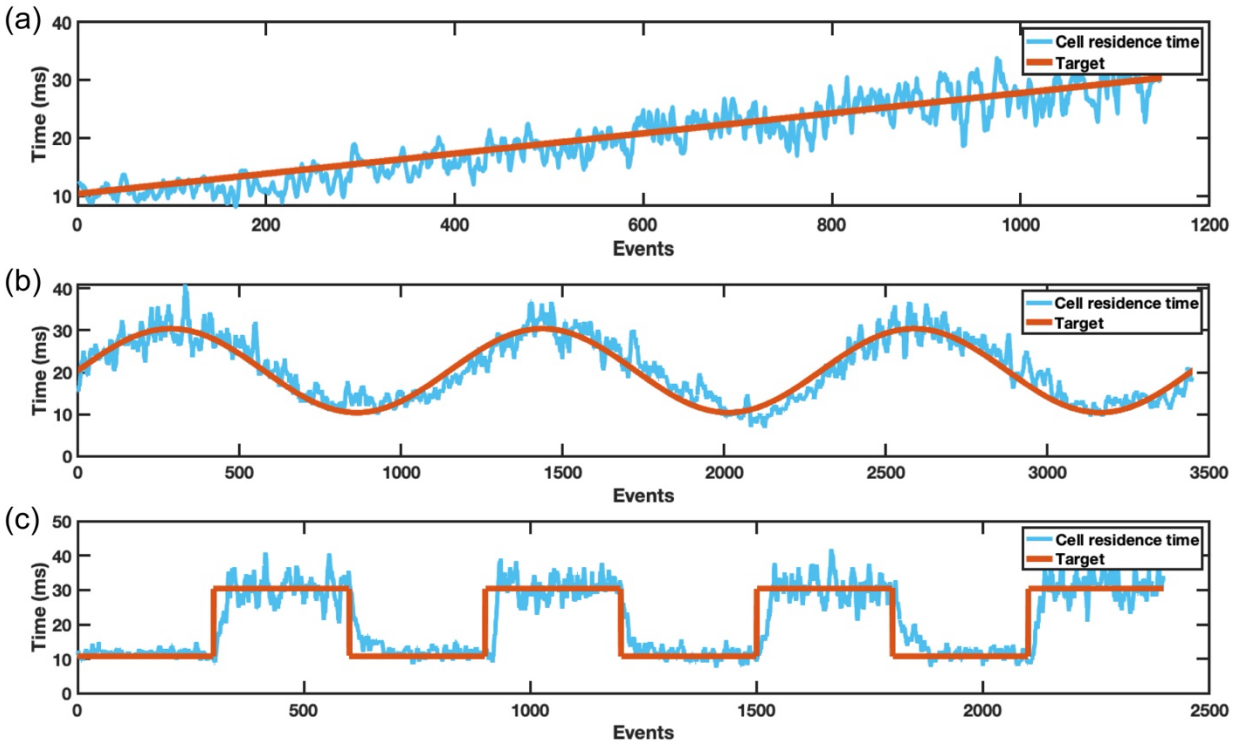

Figure 6: Characterizing the feedback control system by tracking dynamic setpoints in terms of (a) ramp, (b) sine, and (c) square wave. In each case, the cell residence time closed tracks the dynamic setpoint, demonstrating the high accuracy and fast converging speed of the feedback control system.

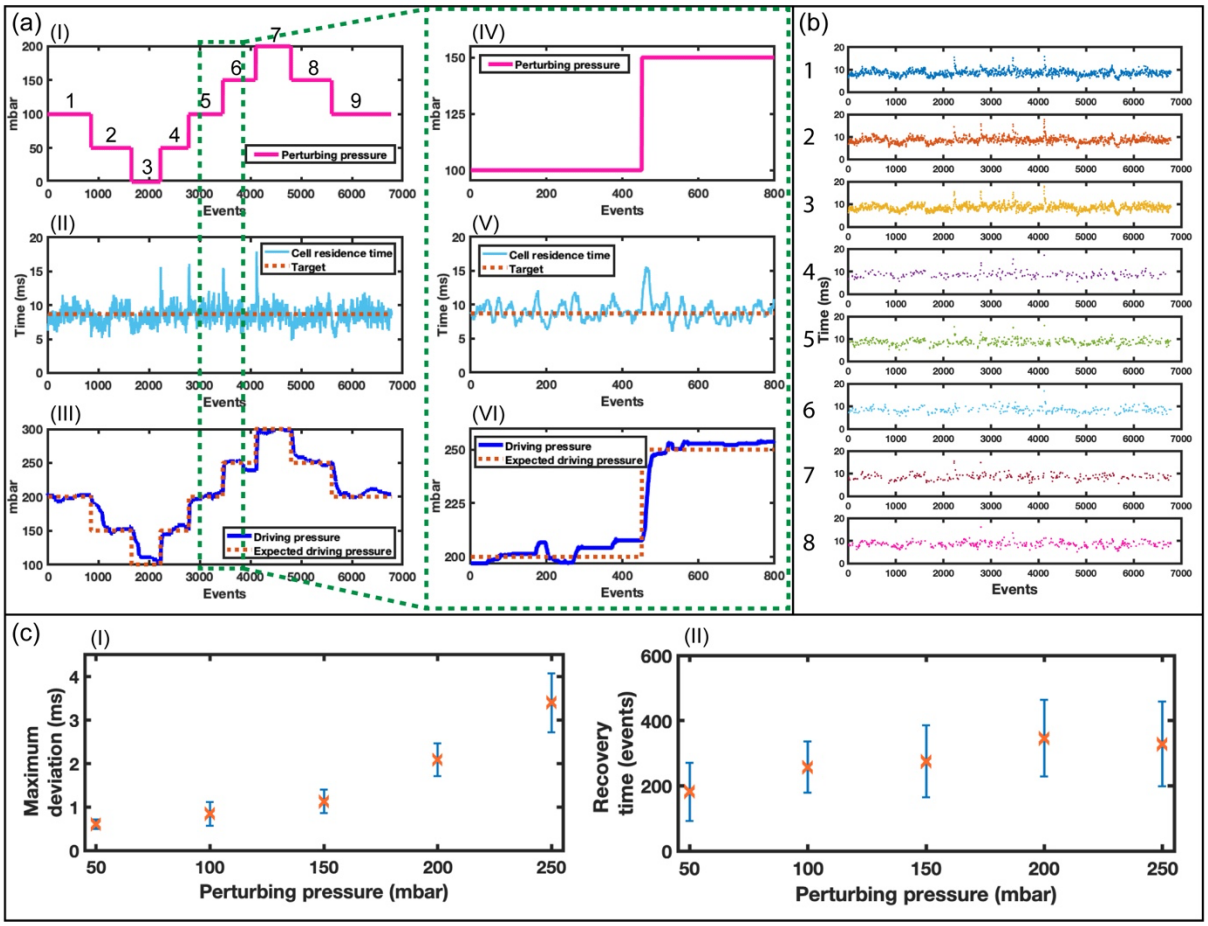

Figure 7: Characterizing the feedback control system under an external perturbation. (a) Left column: System performance under continuous perturbations. (I) The perturbing pressure is introduced from the outlet of the sensor platform and is designed to be a step function with five different values (0, 50, 100, 150, 200 mbar) in nine time periods. (II) The target cell residence time is set to be a constant value at 9 ms. Under the perturbation, the instantaneous cell residence time is maintained around the target, with an abrupt rise and drop when the perturbing pressure changes. (III) The driving pressure is regulated and following the expected value, balancing the perturbation. Right column: A zoomed-in view of the system performance under a perturbation. (IV) The perturbing pressure changes from 100 mbar to 150 mbar at event 450. (V) The cell residence time jumps from 9 ms to 16 ms as the instant decrease of the net forward pressure at event 450. Then the cell residence time recovers to 9 ms within 30 events as a result of the feedback control. (VI) The driving pressure is regulated from 200 mbar to 250 mbar to compensate the pressure introduced from the perturbing pump, maintaining a constant net forward pressure (100 mbar), so that the cell residence time can recover. (b) Cell residence time in terms of different locations (sensor identities). Cells at different locations are regulated to have the same cell residence time. (c) System validation under perturbing pressures ranging from 50 to 250 mbar with 10 repetitive experiments at each pressure. (I) The maximum deviation of the cell residence time (ms) away from the setpoint. (II) The number of events required for the cell residence time to recover to and be stable around the setpoint after the perturbation.

2.4.4 Feedback control under perturbation

To investigate the feedback response under external perturbations, we added another pressure pump (perturbing pump) to the system and monitored the response of the perturbed system. The perturbing pump was connected to the outlet of the microfluidic device to perturb cell flow speed by countering the driving pressure pump connected to the inlet, and the feedback system was engaged to keep the cells flowing at the same speed irrespective of the external perturbation by adjusting the driving pressure. Initially, the net forward pressure was set at 100 mbar with a 200-mbar driving pressure and a 100-mbar perturbing pressure and this condition produced a ~9-ms cell residence time. Sensor and control parameters were chosen as K = 0.1 and W = 10. Later, we modified the perturbing pressure in 50 mbar steps between 0-200 mbar (Figure 7a, I, IV). Despite such a perturbation, the measured instantaneous cell residence time remained at 9 ms, which was the setpoint for our feedback controller (Figure 7a, II, V). Transient ringing in the measured cell residence time coincided with the changes in the perturbation signal as anticipated and was quenched after a few events. The asymmetric ringing of the instantaneous cell residence time at the rising and falling edges of the perturbing pressure was expected due to the non-linear dependence between the cell residence time and the driving pressure (Figure 5b). Finally, comparing the feedback-controlled driving pressure with the perturbing pressure showed that the driving pressure was adjusted to balance the perturbing pressure changes (Figure 7a, III, VI), maintaining a constant net forward pressure. It should be noted that all the automatic adjustments to the driving pressure pump were made based on the aggregate cell residence time data collected from the network of distributed electrical sensors (Figure 7b) without prior knowledge on the perturbation. Taken together, these results showed the ability of the feedback system to successfully adapt to the changing perturbation.

To independently validate the effectiveness of the feedback control in maintaining the cell flow speed within the microfluidic device, we directly measured the flow speed of cells with high-speed microscopy while the device was under perturbation. Cells were randomly sampled for imaging throughout the experiments, and the measurements were compared against the setpoint flow speed (obtained by converting the target cell residence time) (Table 2). The microscopically-measured cell flow speed (n=10) at different time periods (Figure 7a, I) was found to have an average <3.5% deviation from the setpoint flow speed of 35.12 $\mu m/s$ with a 1.39 $\mu m/s$ standard deviation among the measured cell flow speeds. These results proved the ability of the developed feedback-controlled system to maintain a process variable based on direct measurements on cell state under a continuous perturbation.

Time period	1	2	3	4	5	6	7	8	9
Cell flow speed (μm/s)	34.50	34.05	33.15	33.60	32.26	35.84	35.84	36.29	35.39
Accuracy (%)	98.2	97.0	94.4	95.7	91.9	97.9	97.9	96.7	99.2

Table 2: Optically measured cell flow speeds ($\mu m/s$) at nine different time periods during the perturbation experiment closely match the expected cell flow speed (35.12 $\mu m/s$).

We further validated the performance of the system under different perturbing pressures (Figure 7c). Initially, the driving pressure was set to 300 mbar, and the perturbing pressure was set to 0 mbar. Then we changed the perturbing pressure with five different values (50, 100, 150, 200, 250 mbar) and observed the response of the system. We characterized the system regarding two parameters: (1) the maximum deviation represented the maximum distance (ms) between the instantaneous cell residence time and the setpoint (Figure 7c, I); (2) the recovery time (events) represented the number of events required for the instantaneous cell residence time to recover to and be stable around the setpoint (Figure 7c, II). With perturbing pressures ranging from 50 to 250 mbar, the system could successfully recover to the setpoint with increasing maximum deviation and recovery time. As for the breakdown of the feedback loop, our system required a new event (i.e., detection of a cell) to update its settings. If the cell flow were to stop indefinitely before any new measurements, the loop would break.

3. Discussion

We demonstrated a microfluidic system in which the spatiotemporal state of each manipulated cell was continuously monitored with a built-in electrical sensor network, not only as a means for quantitative analysis but also to control and adapt the device operation based on these measurements on the sample under test. Importantly, monitoring of cells within the microfluidic device through electrical signals from the sensor network did not have the redundancy of imaging and hence required less computational resources, which enabled us to implement real-time closed-loop control on process variables. Finally, the fact that measurements for closed-loop control could be performed solely using sensors within the microfluidic device eliminated the need for external instruments such as a microscope or high-speed cameras and demonstrated the feasibility of creating adaptive lab-on-a-chip devices that could be operated outside of research laboratories.

Existing feedback-controlled microfluidic systems either utilize isolated sensors that directly measure a process variable such as pH, temperature, or impedance or utilize arrays of discrete sensors with dedicated readouts for spatial information. In contrast, we could set our feedback loop on multi-dimensional spatiotemporal data from cells within the device while still acting on a one-dimensional electrical waveform. This aspect makes our approach advantageous for implementing adaptive yet low-cost microfluidic cell-based assays. Additionally, we could extract, through computation, cell information including size, speed, and location, any combination of which could be further used as the process variable of the feedback system. When combined with differential manipulation of cells, such spatiotemporal data can be linked to cell biochemical/biophysical properties, further expanding the choice of process variables for the feedback loop.

In terms of electrically tracking cells over the microfluidic device, our deep learning-based demultiplexing scheme offers several advantages over traditional demultiplexing techniques used in code division multiple access (CDMA) telecommunication networks. Traditional approaches employed for demultiplexing coded electrical signals rely on the correlation of the signal with a set of template waveforms to identify specific patterns. While computationally inexpensive, correlation-based demultiplexing requires a special code-set with individual codes

being mutually orthogonal with each other, effectively constraining the design of sensors in the network. In contrast, deep learning-based analysis of the output signal allowed us to identify differentiating features between individual sensor waveforms irrespective of the degree of correlation between them and utilize these differences to rapidly decode the output signal. Besides increased flexibility in design, the ability to train the ConvNets with actual waveforms from sensors rather than relying on model-based templates of ideal square waveforms increases the sensitivity of deep learning-based demultiplexing. It should also be noted that, even though the deep learning model introduced in this work was designed to interpret waveforms from coincidental detection of up to 3 cells, waveforms due to more coincident cells could be resolved, albeit with less accuracy, by modifying the training dataset and the structure of the ConvNets.

The ability to continuously and quantitatively assess manipulation of cells or other particles in a microfluidic device in real-time through built-in sensors and to change the state of the device in response presents exciting opportunities for cell-based microfluidic assays. While this work demonstrated the regulation of cell flow speed under perturbation as a proof of principle, the cell spatiotemporal data generated by networked sensors contained a wealth of information about the sample under test and could be fully utilized to command a variety of actuators internally or externally.[50-56] From the operational point of view, the applications could range from controlling valves to redirect flows based on the instantaneous distribution of cells on the device to the detection of clogged channels or malfunctioning devices. Furthermore, microfluidic systems coupled with different types of stimuli ranging from chemicals to physical transducers could either be automatically tuned to achieve a desired sample response or alternatively be employed to perform automated experiments by sweeping different parameters in a closed-loop setting to extract multi-parametric information from the sample under test.

4. Conclusion

Microfluidics offers cell manipulation capabilities that could not be matched by batch processing and hence is of great interest to create cell-based biomedical assays with high sensitivity and specificity. When coupled with integrated sensors to quantitatively track cell manipulation and software to interpret cell data in real-time, microfluidic devices can be transformed into adaptive platforms, where various process parameters can be regulated through feedback control. In contrast to passive devices often built and tested under controlled conditions with well-characterized samples, adaptive microfluidic systems will not only be less prone to artifacts due to sample heterogeneity, an important requirement for practical utility and translation, but also offer new capabilities for performing experiments/measurements under closed-loop controlled stimuli for basic research.

5. Conflicts of interest

There are no conflicts of interest to declare.

6. Acknowledgment

This work was supported by National Science Foundation, USA (Award no. ECCS 1752170), and the Arnold and Mabel Beckman Foundation, USA (Beckman Young Investigator Award to A.F.S.).

7. References

1. C. W. Shields IV, C. D. Reyes and G. P. Lopez, *Lab Chip*, 2015, **15**, 1230-1249.
2. L. R. Huang, E. C. Cox, R. H. Austin and J. C. Sturm, *Science*, 2004, **304**, 987-990.
3. P. R. C. Gascoyne and J. Vykoukal, *Electrophoresis*, 2002, **23**, 1973-1983.
4. J. Shi, H. Huang, Z. Stratton, Y. Huang and T. J. Huang, *Lab Chip*, 2009, **9**, 3354-3359.
5. D. Robert, N. Pamme, H. Conjeaud, F. Gazeau, A. Iles and C. Wilhelm, *Lab Chip,* 2011, **11**, 1902-1910.
6. Y. Xu, J. A. Phillips, J. Yan, Q. Li, Z. H. Fan and W. Tan, *Anal. Chem.*, 2009, **81**, 7436-42.
7. C. H. Hsu, D. Di Carlo, C. Chen, D. Irimia and M. Toner, *Lab Chip*, 2008, **8**, 2128-2134.
8. Z. Du, N. Colls, K. H. Cheng, M. W. Vaugh and L. Gollahon, *Biosens. Bioelectron*., 2006, **21**, 1991-1995.
9. A. F. Sarioglu, N. Aceto, N. Kojic, M. C. Donaldson, M. Zeinali, B. Hamza, A. Engstrom, H. Zhu, T. K. Sundaresan, D. T. Miyamoto, X. Luo, A. Bardia, B. S. Wittner, S. Ramaswamy, T. Shioda, D. T. Ting, S. L. Stott, R. Kapur, S. Maheswaran, D. A. Haber and M. Toner, Nat. Methods, 2015, **12**, 685–691.
10. W. Zhao, R. Cheng, B. D. Jenkins, T. Zhu, N. E. Okonkwo, C. E. Jones, M. B. Davis, S. K. Kavuri, Z. Hao, C. Schroeder and L. Mao, *Lab Chip*, 2017, **17**, 3097–3111
11. A. W. Wognum, A. C. Eaves and T. E. Thomas, *Arch. Med. Res.*, 2003, **34**, 461-475.
12. F. Bischoff, D. Marquez-Do, D. Martinez, D. Dang, C. Horne, D. Lewis and L. Simpson, *Clin. Genet.*, 2003, **63**, 483-489.
13. G. M. Whitesides, *Nature*, 2006, **442**, 368-373.
14. K. Sato, Y. Tanaka, B. Renberg and T. Kitamori, *Anal. Bioanal. Chem.*, 2009, **393**, 23-29.
15. E. Dressaire and A. Sauret, *Soft Matter*, 2017, **13**, 37-48.
16. A. K. Miri, H. K. Heris, L. Mongeau and F. Javid, *J. Mech. Behav. Biomed*., 2014, **30**, 196-204.
17. S. Kim, K. C. Kim and E. Yeom, *Opt. Lasers Eng*., 2018, **104**, 237-243.
18. Z. Nie, M. Seo, S. Xu, P. C. Lewis, M. Mok, E. Kumacheva, G. M. Whitesides, P. Garstecki and H. A. Stone, *Microfluid. Nanofluidics*, 2008, **5**, 585-594.
19. M. Balas, *IEEE Trans. Automat. Contr*., 1978, **23**, 673-679.
20. C. Li, K. Zhang, X. Wang, J. Zhang, H. Liu and J. Zhou, *Sens. Actuators B Chem*., 2018, **255**, 3616-3622.
21. S. C. C. Shih, R. Fobel, P. Kumar and A. R. Wheeler, *Lab Chip*, 2011, **11**, 535-540.
22. J. Gao, X. Liu, T. Chen, P. Mak, Y. Du, M. Vai, B. Lin and R. P. Martins, *Lab Chip*, 2013, **13**, 443-451.
23. E. Miller, M. Rotea and J. P. Rothstein, *Lab Chip*, 2010, **10**, 1293-1301.
24. Y. Kim, B. Kuczenski, P. R. LeDuc and W. C. Messner, *Lab Chip*, 2009, **9**, 2603-2609.
25. D. T. Eddington, R. H. Liu, J. S. Moore and D. J. Beebe, *Lab Chip*, 2001, **1**, 96-99.
26. L. R. Soenksen, T. Kassis, M. Noh, L. G. Griffith and D. L. Trumper, *Lab Chip*, 2018, **18**, 902-914.
27. J. R. Lake, K. C. Heyde and W. C. Ruder, *PLoS ONE*, 2017, **12**, e0175089.

28. A. I. K. Lao, T. M. H. Lee, I Hsing and N. Y. Ip, *Sens. Actuators A Phys.*, 2000, **84**, 11-17.
29. R. Liu, N. Wang, F. Kamili and A. F. Sarioglu, *Lab Chip*, 2016, **16**, 1350-1357.
30. R. Liu, W. Waheed, N. Wang, O. Civelekoglu, M. Boya, C. H. Chu and A. F. Sarioglu, *Lab Chip*, 2017, **17**, 2650–2666.
31. R. Liu, N. Wang, N. Asmare and A. F. Sarioglu, *Biosens. Bioelectron.*, 2018, **120**, 30-39.
32. N. Wang, R. Liu, N. Asmare, C. H. Chu and A. F. Sarioglu, *Biosens. Bioelectron*., 2021, **174**, 112818.
33. N. Wang, R. Liu, R. Khodambashi, N. Asmare and A. F. Sarioglu, *IEEE 30th International Conference on Micro Electro Mechanical Systems (MEMS), Jan. 22-26*, 2017, Las Vegas, NV, USA, 362-365.
34. W. H. Coulter, *Proc. Natl. Electron. Conf.*, 1956, **12**, 1034-1040.
35. N. Wang, R. Liu and A. F. Sarioglu, *J. Visualized Exp.*, 2017, **121**, e55311.
36. A. Valero, T. Braschler, and P. Renaud, *Lab Chip*, 2010, **10**, 2216-2225.
37. P. Cladé, PyDAQmx: A Python Interface to the National Instruments DAQmx Driver, https://pythonhosted.org/PyDAQmx/.
38. A. C. Muller and S. Guido, *Introduction to Machine Learning with Python: A Guide for Data Scientist*, O'Reilly Media, Inc., Sebastopol, California, 2016.
39. A. Isozaki, J. Harmon, Y. Zhou, S. Li, Y. Nakagawa, M. Hayashi, H. Mikami, C. Lei and K. Goda, *Lab Chip*, 2020, **20**, 3074-3090.
40. C. Honrado, J. S. McGrath, R. Reale, P. Bisegna, N. S. Swami and F. Caselli, *Anal. Bioanal. Chem.*, 2020, **412**, 3835-3845.
41. E. Sharma, R. C. Deo, R. Prasad, A. V. Parisi and N. Raj, *IEEE Access*, 2020, **8**, 209503-209516.
42. Y. C. Chen, Z. Zhang and E. Yoon, *Anal. Chem*., 2020, **92**, 7717-7724.
43. N. Wang, R. Liu, N. Asmare, C.-H. Chu and A. F. Sarioglu, *Lab Chip*, 2019, **19**, 3292–3304
44. N. Wang, R. Liu, N. Asmare, D. B. Anandakumar and A. F. Sarioglu, *Proceedings of 20th International Conference on Solid-State Sensors, Actuators and Microsystems & Eurosensors XXXIII (TRANSDUCERS & EUROSENSORS XXXIII), June 23-27*, 2019, Berlin, Germany, 202-205.
45. R. W. DeBlois and C. P. Bean, *Rev. Sci. Instrum*., 1970, **41**, 909–916.
46. C. Honrado, P. Bisegna, N. S. Swami and F. Caselli, *Lab Chip*, 2021, **21**, 22-54.
47. D. R. Gossett, W. M. Weaver, A. J. Mach, S. C. Hur, H. T. K. Tse, W. Lee, H. Amini and D. Di Carlo, *Anal. Bioanal. Chem.*, 2010, **397**, 3249-3267.
48. K. H. Ang, G. C. Y. Chong and Y. Li, *IEEE Trans. Contr. Syst. T.*, 2005, **13**, 559-576.
49. J. A. Backer, C. P. Lowe, H. C. J. Hoefsloot and P. D. ledema, *J. Chem. Phys*., 2005, **122**, 154503.
50. O. Civelekoglu, N. Wang, M. Boya, T. Ozkaya-Ahmadov, R. Liu and A. F. Sarioglu, *Lab Chip*, 2019, **19**, 2444-2455.
51. O. Civelekoglu, R. Liu, M. Boya, C. H. Chu, N. Wang and A. F. Sarioglu, *Proceedings of 19th International Conference on Solid-State Sensors, Actuators and Microsystems (TRANSDUCERS), June 18-22*, 2017, Kaohsiung, Taiwan, 480-483.
52. O. Civelekoglu, N. Wang, M. Boya, T. Ozkaya-Ahmadov, R. Liu and A. F. Sarioglu, *Proceedings of 20th International Conference on Solid-State Sensors, Actuators and Microsystems & Eurosensors XXXIII (TRANSDUCERS & EUROSENSORS XXXIII), June 23-27*, 2019, Berlin, Germany, 975-978.

53. R. Liu, C. H. Chu, N. Wang, T. Ozkaya-Ahmadov, O. Civelekoglu, D. Lee, A K M Arifuzzman and A. F. Sarioglu, *Small*, 2019, **15**, 1904732.
54. R. Liu, N. Wang, C. H. Chu and A. F. Sarioglu, *Proceedings of 19th International Conference on Solid-State Sensors, Actuators and Microsystems (TRANSDUCERS), June 18-22*, 2017, Kaohsiung, Taiwan, 2115-2118.
55. R. Liu, A K M Arifuzzman, N. Wang, O. Civelekoglu and A. F. Sarioglu, *J. Microelectromech. Syst*., 2020, **29**, 942-947.
56. N. Asmare, A K M Arifuzzman, N. Wang, M. Boya, R. Liu and A. F. Sarioglu, *Proceedings of 20th International Conference on Solid-State Sensors, Actuators and Microsystems & Eurosensors XXXIII (TRANSDUCERS & EUROSENSORS XXXIII), June 23-27*, 2019, Berlin, Germany, 948-951.